ELSEVIER

Journal of Neuroscience Methods 171 (2008) 153–164

JOURNAL OF NEUROSCIENCE METHODS

www.elsevier.com/locate/jneumeth

Automated detection and analysis of foraging behavior in *Caenorhabditis elegans*

Kuang-Man Huang [a,*], Pamela Cosman [a], William R. Schafer [b]

[a] *Department of Electrical and Computer Engineering, University of California at San Diego, La Jolla, San Diego, CA 92093-0407, USA*
[b] *Cell Biology Division, MRC Laboratory of Molecular Biology, Cambridge CB2 0QH, UK*

Received 4 December 2007; received in revised form 31 January 2008; accepted 31 January 2008

Abstract

Foraging is a rapid, side-to-side movement of the nose generated by *Caenorhabditis elegans* as it explores its environment. In this paper, we present an automated method to detect and analyze foraging behavior of *C. elegans* in a video sequence. Several morphological image-processing methods are used to locate the precise nose position of the worm in each image. Then foraging events are detected by measuring the bending angle of the nose and investigating the overall bending curve using periodograms. We measure foraging-related parameters which have not previously been studied. The algorithm has applications in classifying and characterizing genetic mutations associated with this behavior.

Keywords: *Caenorhabditis elegans*; Foraging; Image processing; Automated detection; Periodogram

1. Introduction

The nematode *Caenorhabditis elegans* is widely used in studies of nervous system function and behavior. *C. elegans* is particularly useful as a neurobiological model because of its completely sequenced genome and its amenability to classical and molecular genetics. In addition, it has a compact and well-defined nervous system, in which each neuron (of 302 in total) has been individually identified and characterized at the level of synaptic connectivity (White et al., 1986). In principle, it is possible to identify mutants with specific behavioral abnormalities and understand mechanistically how individual gene products act within the context of the neural circuitry to produce these behavioral phenotypes.

Despite its anatomically simple nervous system, *C. elegans* is capable of surprisingly diverse patterns of behaviors. While some of these, such as feeding, egg-laying, and defecation, are mechanically simple (Avery and Thomas, 1997; Schafer, 2006), other behaviors involve complex motor programs requiring intricate coordination of muscle groups. These include locomotor behaviors such as backward and forward crawling, swimming, and copulation (Barr and Garcia, 2006). Recently, there has been increasing interest in quantitatively characterizing and modeling these more complex motor programs (Chen et al., 2006; Karbowski et al., 2007); however, significant questions remain regarding the nature of these behaviors and how they are generated by the nervous system.

A *C. elegans* behavior that has received comparatively little attention is foraging. Foraging is a term used to describe rapid, side-to-side movements of the nose generated by the worm as it explores its environment. Several neurons, including the OLQ and IL1 sensory neurons and the RMG motorneurons, have been shown to be required for this behavior (Driscoll and Kaplan, 1997; Kaplan and Horvitz, 1993). Various genes conferring a foraging abnormal ("Fab") phenotype have also been identified; for example, the AMPA-type glutamate receptor gene *glr-1* is required for foraging (Hart et al., 1995), and the G-protein alpha-subunit gene *goa-1* as well as other genes in the Go/Gq signaling pathway affect the rate of foraging (Alkema et al., 2005; Segalat et al., 1995). However, the precise nature of the foraging movements in wild type and mutant strains has not been characterized.

Studies of foraging behavior have relied exclusively on the time-consuming analysis of video recordings by human observers. For this reason, we use an automated system (Baek et al., 2002; Cronin et al., 2005; Feng et al., 2004; Geng et al., 2004; Hoy et al., 1996, 1997) consisting of a tracking microscope and image-processing software to follow and analyze the

* Corresponding author.
E-mail address: houston21@hotmail.com (K.-M. Huang).

0165-0270/$ – see front matter © 2008 Elsevier B.V. All rights reserved.
doi:10.1016/j.jneumeth.2008.01.027

movements of individual animals at high magnification. Using video data collected using an automated tracking system, we have been able to reliably detect foraging events and provide the first quantitative description of foraging movements in *C. elegans*. Fourier analysis of these data identifies characteristic frequencies that can be used to parameterize foraging patterns. These analyses provide more precise methods for defining the effects of specific genes and neurons on *C. elegans* behavior. This paper is organized as follows. In Section 2, we describe the foraging detection algorithm, including image acquisition and pre-processing. In Section 3, we evaluate the algorithm by testing it on a variety of videos of mutant worms, and verifying the results with manual observations. We also describe how to extract foraging-related parameters, and we combine these parameters with Fourier analysis to analyze foraging behavior. Discussion and conclusions appear in Sections 4 and 5.

2. Materials and methods

2.1. Strains and culture methods

C. elegans strains were maintained as described (Brenner, 1974). For all assays, 4-day-old young adults were used; fourth-stage larvae were picked the evening before the experiment and tracked the following morning. Plates used for tracking were prepared by spreading one drop of a saturated LB (Luria broth) culture of *Escherichia coli* strain OP50 onto NGM (nematode growth medium) agar plates. Experimental animals were allowed to acclimate for 5 min before tracking. We used wild type worms and the following mutants: *dgk-1(nu62); glr-1(n2361); goa-1(n1143); trpa-1(ok999)*.

2.2. Acquisition of image data

C. elegans locomotion was tracked with a Zeiss Stemi 2000-C microscope mounted with a Cohu High Performance CCD video camera essentially as described (Geng et al., 2004). The microscope was outfitted for brightfield illumination from a 12 V 20 W halogen bulb reflected from a flat mirror positioned at an angle of approximately 45°. A tracker controlled by a Dell 1.0 GHz Pentium-III desktop computer was used to maintain the worms in the center of the optical field of the microscope during observation. To record the locomotion of an animal, image frames of the animal were captured at a frequency of 30 Hz and then saved as AVI video files (encoded with mpeg4v2) for at least 1 min ($30 \times 60 = 1800$ images per video). Next, we binarized the image using an adaptive threshold (the average value minus three times the standard deviation) and found the connected component with the largest area. The original image was then trimmed to the smallest axis-aligned rectangle that contained this component, and saved as eight-bit grayscale data. The dimensions of each image, and the coordinates of the upper left corner of the rectangle box containing the worm body in the tracker field were also recorded simultaneously. The microscope was fixed to its largest magnification (50×) during observation. The number of pixels per millimeter was fixed at 312.5 pixel/mm for all worms.

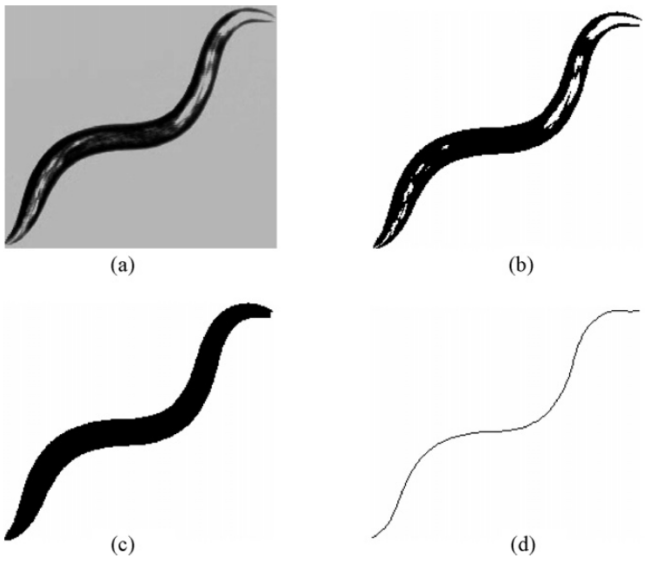

Fig. 1. (a) Gray level image acquired from a video sequence, (b) corresponding binary image after thresholding, (c) binary image after hole filling and closing operator and (d) skeleton after skeletonizing and pruning algorithm.

2.3. Image pre-processing

To facilitate analysis, the grayscale images were subjected to preliminary image processing to generate a simplified representation of the body (Geng et al., 2004). First any images which were snapped when the stage was moving (the current coordinate of the stage was different from the previous coordinate) were discarded because these images were usually blurry. Then for each good image frame (Fig. 1a), an adaptive local thresholding algorithm (Fig. 1b) followed by a morphological closing operator (binary dilation followed by erosion) was used. As described in (Geng et al., 2004), a corresponding reference binary image was also generated by filling holes inside the worm body based on image content information. The difference between these two binary images provided a good indication of which image areas are worm body and which are background (Fig. 1c). Following binarization, a morphological skeleton was obtained (Fig. 1d) (Geng et al., 2004; Gonzalez and Woods, 2002).

2.4. Locating the worm nose

After a morphological skeleton is obtained, 25 evenly spaced skeleton points are extracted. The two end points on the skeleton represent the head and tail positions (Fig. 2a). Using the

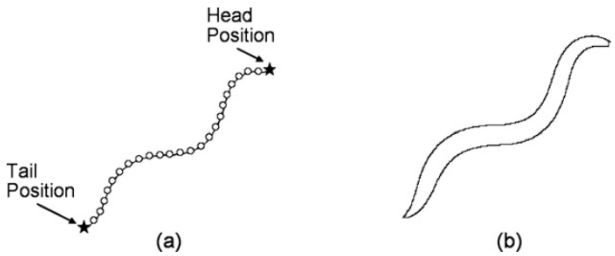

Fig. 2. (a) Skeleton with 25 sampled skeleton points and (b) the exterior contour of the worm body.

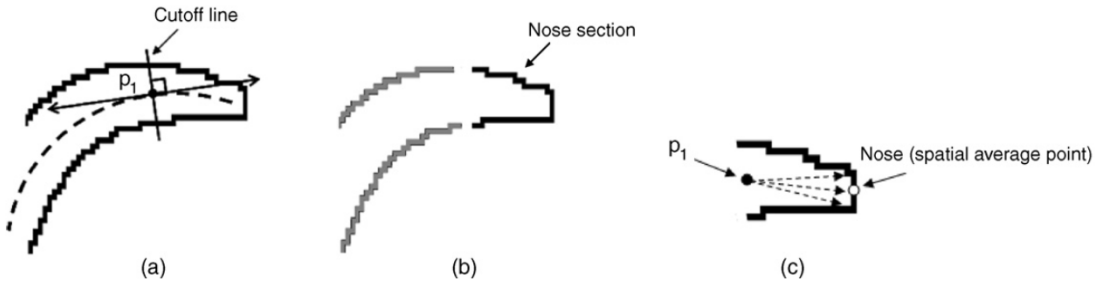

Fig. 3. (a) Placing a cutoff line at the first skeleton point p_1 perpendicular to the tangent line at p_1, (b) isolating the nose section from the rest of the body and (c) computing the spatial average from the 10 points furthest from p_1.

approach in (Geng et al., 2004), the head is recognized for entire video sequences using the brightness (the head is usually brighter than the tail) and the distance moved between the current frame and the previous frame (the head usually moves more than the tail) for the two end points. However, the head position on the skeleton as calculated in (Geng et al., 2004) is not precisely the same as the nose position recognized in the original grayscale image. To detect foraging events which are related to subtle nose movement, we need to locate the nose position more precisely. First we obtain the exterior boundary of the worm body by eroding it with a 3×3 square structuring element and then performing the set difference between the binary image and its erosion (Fig. 2b). A cutoff line is then placed which passes through the first skeleton point p_1 and is perpendicular to the skeleton tangent line at p_1. The cutoff line cuts the exterior contour into two parts (Fig. 3a). The smaller part which contains the head point is the nose section of the contour and will be isolated from the rest of the body (Fig. 3b). We compute the distances between the point p_1 and each pixel on the nose section of the contour. The 10 points having the longest distances from the point p_1 are selected and used to compute the spatial average point p_n, which we define to be the position of the nose (Fig. 3c).

2.5. Foraging event detection

In (Kindt et al., 2007), a foraging movement is defined as a complete cycle of movements by the tip of the nose from the ventral side through the dorsal extreme or vice versa during time intervals when the animal was moving forward (Fig. 4). Sometimes worms can move either forwards or backwards depending on the direction in which the sinusoidal waveform is propagated down the body. This backward movement is defined as a reversal. Omega bends occur when the worm takes on the shape of a capital omega and curves its head around to touch the middle part of its body then sharply bends away from its body. Based on the definition of foraging in (Kindt et al., 2007), any detected foraging events during reversals or omega bends will not be counted as foraging events. We used the method in (Huang et al., 2006) to detect reversals and omega bends automatically.

To investigate this kind of side by side nose movement in a video, we measure the nose bending angle b between the segments (p_n, p_1) and (p_1, p_2) where p_1, p_2 are the first and second skeleton points from the head and p_n is the nose position (Fig. 4). The nose bending direction is defined to be left if $b > 0$ and to be right if $b < 0$. Fig. 5 contains plots of $b(t)$ which show nose bending angle over time from a video. Here t is the frame index. The overall curve is in a rough sinusoidal shape because the worm generally moves in a sinusoidal wave. We can also notice that there are some dips and peaks (extrema) marked on the curve in Fig. 5a. Each set of three consecutive extrema (consisting either of two local maxima and the local minimum between them, or else of two local minima and the local maximum between them) represents a side-to-side motion of the nose and is therefore considered to be a candidate foraging event. From the beginning of each video, we search for and examine each set of three consecutive extrema. We denote the first, second, and third local extreme values (in a time-wise order) to be its start point SP, middle point MP, and end point EP, respectively. A set of three consecutive extrema is considered to be a foraging event if that

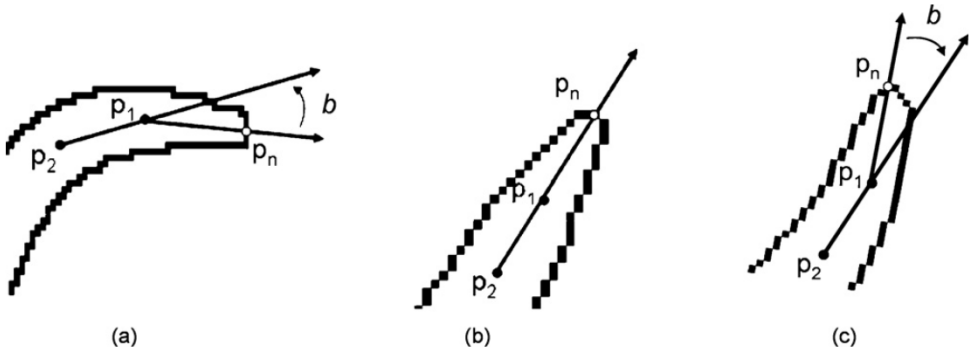

Fig. 4. Computing the nose bending angle b in every frame: (a) nose bends to the right of the midline, (b) nose points straight ahead and (c) nose bends to the left of the midline.

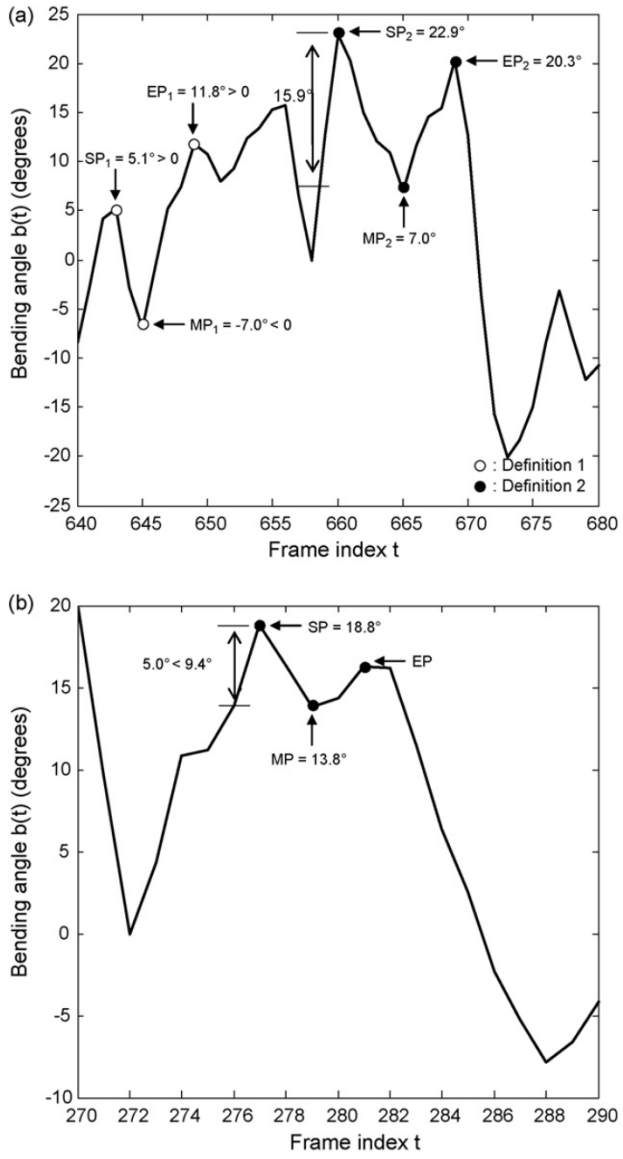

Fig. 5. (a) An example of nose bending angle over time from a video. A detected foraging event of definition 1 is shown in white dots and the other event of definition 2 ($\alpha = 0.5$) is shown in black dots and (b) an example of a non-foraging event.

segment of the video does not contain any bad frames (frames discarded due to stage movement) and if either of the following two criteria is satisfied:

(1) Sign[SP] = sign[EP] = −sign[MP]: when this criterion is satisfied, it means that the worm's nose is waving across the middle line ($b = 0$) to reach the other side then waving back to accomplish a complete foraging movement. An example of a foraging event of this kind is shown by white dots (SP_1, MP_1 and EP_1) in Fig. 5a.

(2) Sign[SP] = sign[EP] = sign[MP] and abs[SP−MP] > αabs[SP]: when this criterion is satisfied, it means that even though the worm's nose does not cross the middle line, the moving angle of the nose is still larger than some fraction α of its starting bending angle which, depending on α, is noticeable enough to be considered to be a foraging event. An example of a foraging event of this kind (e.g. $\alpha = 0.5$) is shown by black dots (SP_2, MP_2 and EP_2) in Fig. 5a. The angle difference between SP_2 and MP_2 is 15.9° which is larger than $0.5 \times SP_2 = 11.45°$. Fig. 5b shows an event that does not satisfy either of the above two criteria (when $\alpha = 0.5$).

Once a set of three consecutive extrema is decided to be a foraging event, the search for additional foraging events will start from the end point EP of the previous event to avoid having foraging events overlapping.

3. Results

In this section, first we present verification results assessing the robustness of our foraging detection algorithm and decide the best value of α for our algorithm. Then we analyze foraging behavior in the following steps: (1) we start by investigating the previously obtained nose bending signals by estimating their power spectra, (2) some parameters such as waving amplitude and frequency (which will be described in detail later) are extracted from detected foraging events and (3) then we combine the obtained parameters with power spectrum analysis and use *t*-tests to study the similarities of foraging behavior between wild type and each of the four mutant types. The experiments were implemented in Matlab on a 2.33 GHz Pentium-IV desktop computer.

3.1. Verification of the foraging detection algorithm by human observers

Our algorithm for the detection of foraging events was tested on 25 (five videos for each strain) 1-min videos (30 Hz). First, a trained human observer examined all the videos to locate all the foraging events. By applying the above algorithm with α varying from 0 to 1, the performance result is shown as a receiver operating characteristic (ROC) curve (Metz, 1978) in Fig. 6 and Table 1. There is a sharp bend in the ROC curve when $\alpha = 0.5$ (at which point the true positive fraction is over 90% while the false positive fraction is less than 10%), indicating $\alpha = 0.5$ is the best for this algorithm. For $\alpha = 0.5$, the foraging event detection results for individual strains are given in Table 2.

3.2. Fourier analysis of foraging events

In another experiment, we used spectral analysis to investigate the foraging behavior of each strain. In particular, we estimated the power spectrum for each strain from 150 videos (30 videos for each strain) by averaging multiple periodograms (Welch–Bartlett method, Welch, 1967). The periodogram is an estimator of the power spectrum, introduced by Schuster (Manolakis et al., 2000). To calculate the periodogram for each strain, first we subdivided each bending angle signal $b_p(t)$ ($1 \le p \le 30$ videos for each strain) into small segments in a sliding window and overlapping fashion. The window used in this

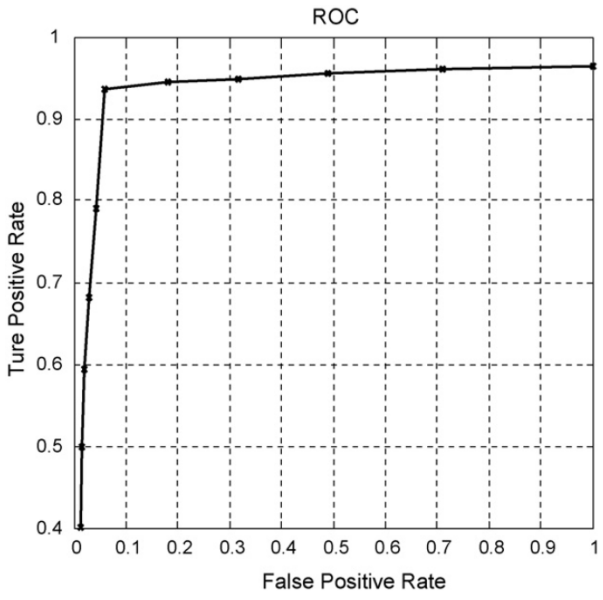

Fig. 6. A plot of the receiver operating characteristic (ROC) curve with α varying from 0 to 1.

experiment is a Hamming window of duration $L=30$ with values $w(m) = 0.54 - 0.46\cos(2\pi m/29)$ for $m=0, 1,\ldots, 29$. We set $D=20$ ($D<L$) to be an offset distance to make the segments overlap and create more segments, and let K_p be the number of segments in the pth video, which changed with different videos (for example, a video glr-1_001 with 1745 frames was divided into 1745/D $\approx$ 87 segments). Then the qth segment of the pth video consists of the following L values:

$$b_{pq}(m) = b_p(qD+m)w(m) \quad 0 \le m \le L-1, \quad 0 \le q \le k_p - 1$$

The estimated power spectrum (periodogram) $\hat{B}_{pq}(e^{j\omega})$ of the qth segment of the pth video can be calculated using the discrete Fourier transform as follows:

$$\hat{B}_{pq}(e^{j\omega}) \equiv \frac{1}{L}|B_{pq}(e^{j\omega})|^2 = \frac{1}{L}\left|\sum_{m=0}^{L-1} b_{pq}(m)e^{-j\omega m}\right|^2$$

The spectrum estimate of each strain was obtained by averaging the periodograms from all of its $\sum_{p=1}^{30} K_p$ curves as follows:

$$\hat{B}(e^{j\omega}) = \frac{1}{\sum_{p=1}^{30} K_p}\sum_{p=1}^{30}\sum_{q=1}^{K_p}\hat{B}_{pq}(e^{j\omega}) = \frac{1}{\sum_{p=1}^{30} K_p}\sum_{p=1}^{30}\sum_{q=1}^{K_p}\frac{1}{L}|B_{pq}(e^{j\omega})|^2 = \frac{1}{\sum_{p=1}^{30} K_p}\sum_{p=1}^{30}\sum_{q=1}^{K_p}\frac{1}{L}\left|\sum_{m=0}^{L-1} b_{pq}(m)e^{-j\omega m}\right|^2$$

We also obtained a different averaged spectrum only from segments where foraging events happened. In this case, after foraging events were detected, a Hamming window was placed

Table 1
The false positive, true positive, false negative, and true negative values for the ROC curve

Rate of non-foraging events detected as foraging (false positive)	Rate of foraging events detected as foraging (true positive)	Rate of foraging events detected as non-foraging (false negative)	Rate of non-foraging events detected as non-foraging (true negative)	α
1.0000	0.9637	0.0363	0	0
0.7116	0.9609	0.0391	0.2884	0.1
0.4890	0.9554	0.0446	0.5110	0.2
0.3176	0.9491	0.0509	0.6824	0.3
0.1819	0.9442	0.0558	0.8181	0.4
0.0597	**0.9351**	**0.0649**	**0.9403**	**0.5**
0.0435	0.7901	0.2099	0.9565	0.6
0.0287	0.6820	0.3180	0.9713	0.7
0.0205	0.5941	0.4059	0.9795	0.8
0.0153	0.4986	0.5014	0.9847	0.9
0.0119	0.4010	0.5990	0.9881	1.0

The highlighted row is the final α used in the foraging detection.

Table 2
Verification results of each strain for the foraging detection algorithm ($\alpha=0.5$)

Worm type	*dgk1(nu62)*	*glr1(n2361)*	*goa1(n1143)*	*trpa1(ok999)*	*wild type*
Total frames	5513	8105	5387	6709	6273
Detected foraging	243	354	302	268	299
Foraging not detected	8.8% (21)	7.9% (27)	3.7% (11)	4.0% (10)	7.9% (24)
Real foraging %	90.2% (219)	89.0% (315)	94.0% (284)	90.3% (242)	94.0% (281)

The first row shows the mutant type. The second row shows the number of frames where the worms were moving forward. The number of events detected by the algorithm is listed in row 3. The number of foraging events missed is listed in row 4. The number of detected events which are real foraging events is listed in row 5.

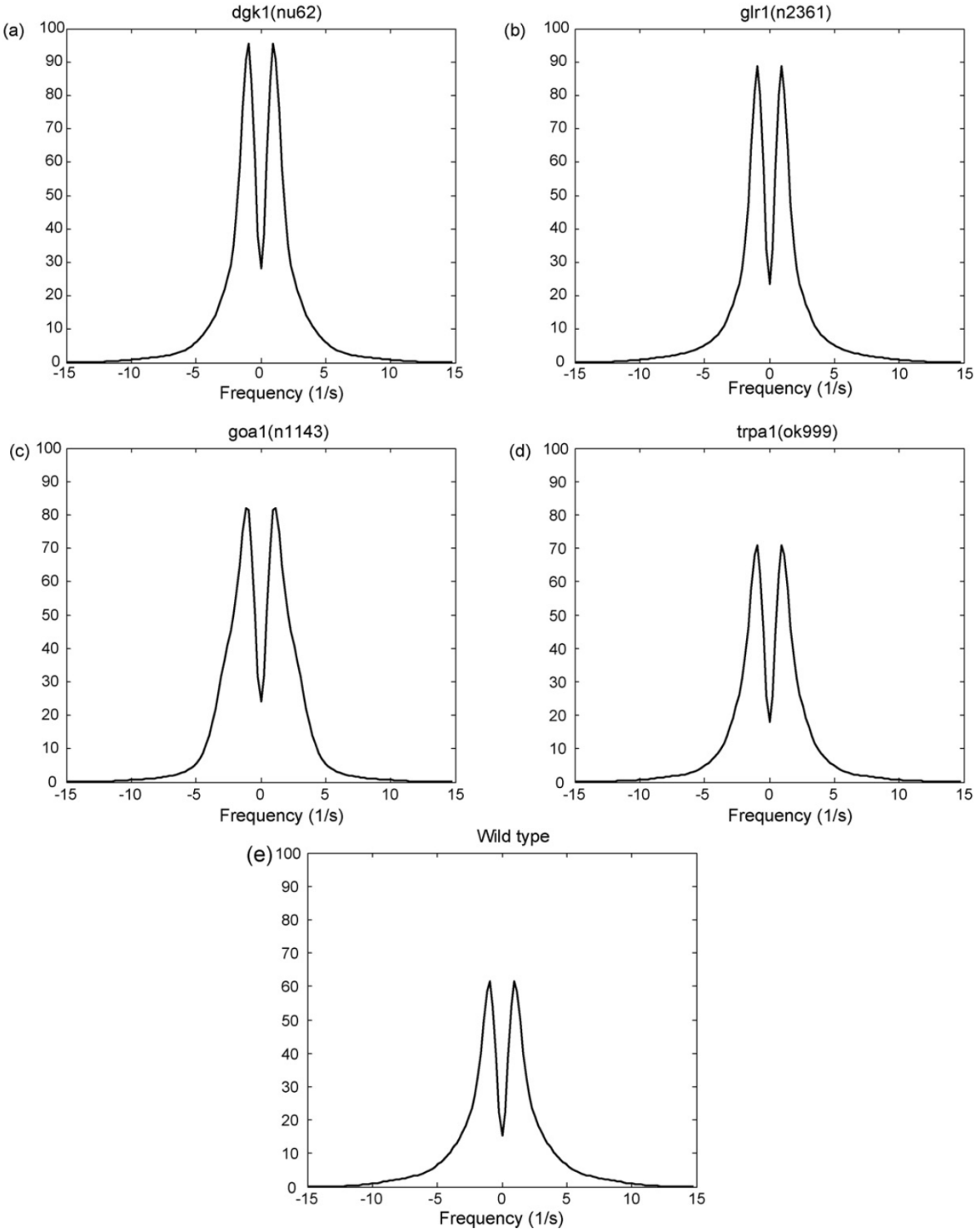

Fig. 7. The estimated overall power spectrum for all strains: (a) *dgk-1*, (b) *glr-1*, (c) *goa-1*, (d) *trpa-1* and (e) wild type.

at each foraging event (the center of the window points to the center of the foraging event) and the periodogram of each event was computed. For each strain, the foraging spectrum is averaged from all N periodograms where N is the number of detected foraging events for the strain. The results of Fourier analysis of foraging behaviors are in Figs. 7 and 8. Fig. 7 includes spectra of complete videos and Fig. 8 shows spectra from foraging events only. In Fig. 7, we can see that there is a main frequency for each strain which corresponds to the frequency of the approximately sinusoidal worm body wave. These main components also exist in Fig. 8. But we can also find subtle bumps on the outer sides of the main component which are caused by the foraging. To observe these bumps more clearly, we take the ratio of the spectra in Fig. 8 to those in Fig. 7. The results are shown in

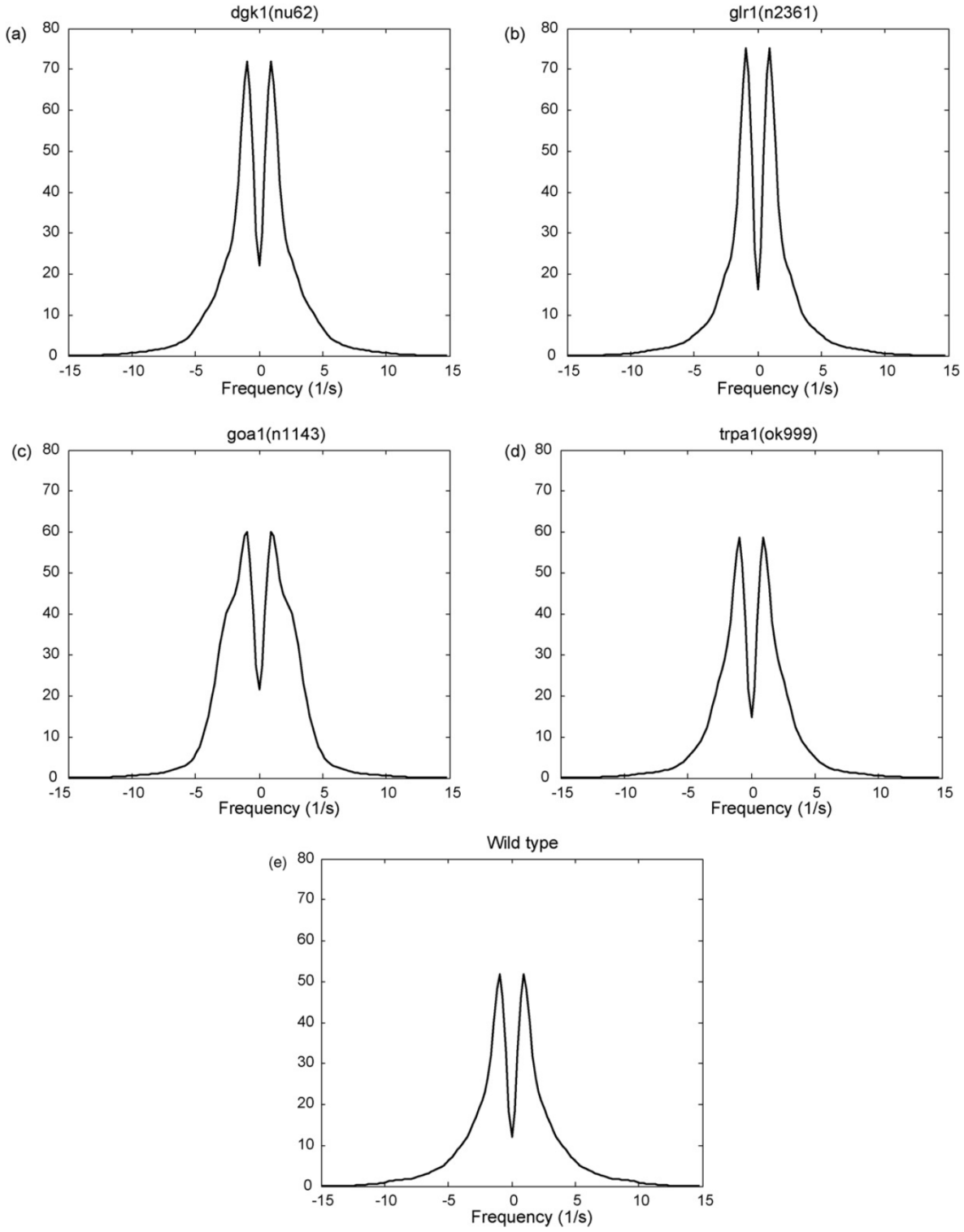

Fig. 8. The estimated power spectrum from detected foraging events for all strains: (a) *dgk-1*, (b) *glr-1*, (c) *goa-1*, (d) *trpa-1* and (e) wild type.

solid curves in Fig. 9. We also computed the ratio of the spectrum generated from randomly chosen segments to the spectrum generated from the overall video and the results are shown in long-dashed curves in Fig. 9. We can see that the curve from randomly chosen segments is close to 1 and does not have any obvious peak at any frequency.

3.3. Statistical analysis of foraging events

After foraging events were detected for each strain, we extracted several basic features from all detected events from bending curves (as shown in Fig. 5). These include: waving amplitude, initial waving direction, time interval between adja-

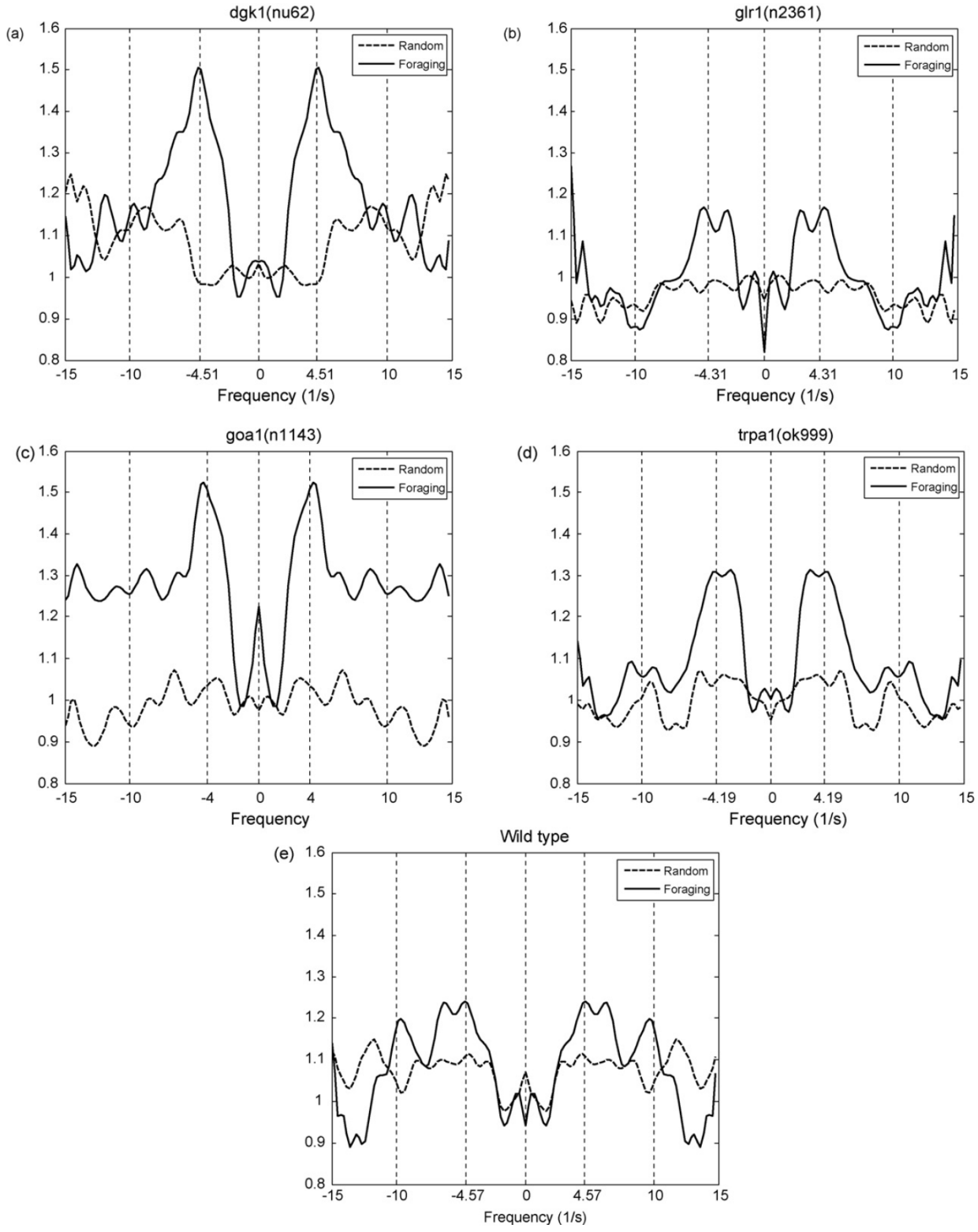

Fig. 9. For each mutant type, we compute the ratio of Fig. 8 to Fig. 7 (solid line) as well as the ratio of the spectrum generated from randomly chosen segments to the spectrum generated from the overall video (long-dashed line).

Table 3
Foraging-related features extracted from all events detected by the algorithm

Worm type	*dgk-1(nu62)*	*glr-1(n2361)*	*goa-1(n1143)*	*trpa-1(ok999)*	*wild type*
Total foragings	1669	1604	1820	1480	1789
Left	813	841	911	735	927
Right	856	763	909	745	862
Amplitude AVE	15.13	14.91	19.26	15.71	14.15
Amplitude STD	9.30	8.27	11.14	9.00	8.34
Interval AVE	0.199	0.386	0.171	0.249	0.216
Interval STD	0.245	0.465	0.206	0.325	0.293
Frequency AVE	4.51	4.31	4.00	4.19	4.57
Frequency STD	1.58	1.64	1.57	1.66	1.61

The first row shows the mutant type. The second row shows the total number of foraging events for each strain detected by the algorithm. The third and fourth rows show the number of foraging events which start respectively from the left and right side of the body. The mean values and standard deviation values of features are listed in rows 5 and 6 (waving amplitude), rows 7 and 8 (time interval between adjacent events) and rows 9 and 10 (the frequency of nose waving during foraging events).

cent foraging events, and the frequency of nose waving during an individual foraging event. These features are described in detail as follows:

(1) *Wave amplitude*: It is defined to be the depth of nose bending (in degrees) during a foraging event. Once a foraging event is found, we compute $\{\text{abs}[\text{SP}-\text{MP}]+\text{abs}[\text{EP}-\text{MP}]\}/2$ to be its amplitude.
(2) *Initial waving direction*: Is the side from which the worm starts a foraging event ($\text{SP}>0$ is defined to be left and $\text{SP}<0$ is defined to be right).
(3) *Time interval between adjacent foraging events*: For adjacent events, this parameter is defined to be the time interval between the end point EP of the first event and the start point SP of the second event.
(4) *Frequency of individual foraging event*: This parameter represents the inverse of the period of an individual foraging event, which can be expressed as $1/T$ where T is the time length between the start point SP and the end point EP of the event.

The mean values and standard deviation values of each feature were computed for each strain and the results are listed in Table 3. The first row shows the mutant type. The second row shows the number of foraging events detected by the algorithm. The third and fourth rows show the number of foraging events which start respectively from the left and right side of the body. The mean values and standard deviation values of features are listed in rows 5 and 6 (waving amplitude), rows 7 and 8 (time interval between adjacent events) and rows 9 and 10 (the frequency of nose waving during foraging events).

We compared the results in Table 3 to the previously obtained power spectrum ratios for each strain. Among these five mutant types, *goa-1* has the largest average amplitude and its curve in Fig. 9 generally has higher values than the other mutant types. The average foraging frequencies in Table 3 computed from all detected events for *dgk-1* and *goa-l* are also very close to their peak values in Fig. 9a and c. *glr-1*, *trpa-1* and wild type have two nearly equal maximal peak values in Fig. 9b, d and e, but their average foraging frequencies still locate within the main lobes of the spectra in Fig. 9. Their standard deviation values of foraging frequency are also larger than those for *dgk-1* and *goa-1*.

In order to study the similarities of foraging behavior between mutants, we generate scatter plots of each parameter (amplitude, interval and frequency as in Table 3) for wild type and each of the four mutants. The mean values of three parameters of each video are computed. The scatter plot of each parameter is generated by using each video as a data point (Fig. 10). From these plots, we make three observations: (1) for mutant types *dgk-1* and *goa-1,* which are hyperactive for locomotion and foraging, their time intervals between adjacent events are almost all within a range from 0.1 to 0.3 s. Mutant types *glr-1* and *trpa-1* which forage more slowly have much wider distribution with many data points having larger values than other mutant types, (2) *goa-1* has generally higher values in the plot of amplitude, while most of the data points of other mutant types are within a range of 10–20° and (3) *dgk-1, glr-1* and wild type have similar ranges of

Table 4
The average number of foraging events within 10 s

Worm type	*dgk-1(nu62)*	*glr-1(n2361)*	*goa-1(n1143)*	*trpa-1(ok999)*	*wild type*
Total frames	34,136	43,728	32,379	35,010	36,835
Detect foraging	1,669	1,604	1,820	1,480	1,789
No. of foraging in 10 s	14.67	11.00	16.86	12.68	14.57
Chi-Square (p-value)	1,067 (≈0)	1,016 (≈0)	1,203 (≈0)	928 (≈0)	1,190 (≈0)

The first row lists the mutant type and the second row lists the total number of frames in which the worms were moving forward. The third row lists the number of foraging events detected by the algorithm. The fourth row shows the average number of foraging events in 10 s. The bottom row shows the Chi-Square and p-values of the test for periodicity for each strain.

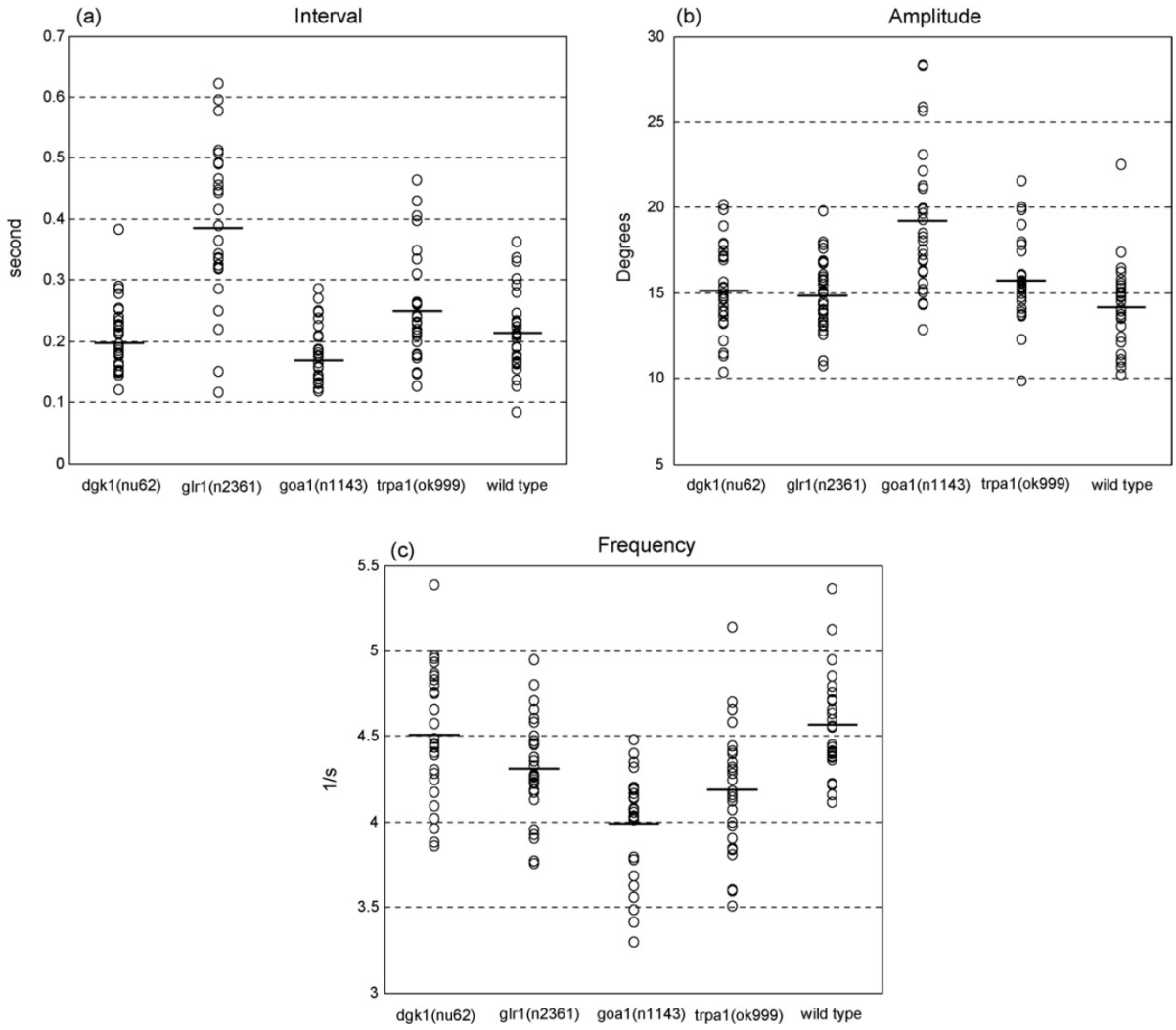

Fig. 10. The scatter plot of three parameters for all strains: (a) time interval between adjacent events, (b) amplitude and (c) frequency of individual foraging event. The solid lines show the overall mean values.

distribution for frequency of individual foraging event (4–51/s) and *goa-1* has lower distribution in the plot which matches the result in Table 3.

We also computed the foraging rate, which is defined in (Kindt et al., 2007) to be the number of foraging events within 10 s, for each strain and the results are listed in Table 4. The first row lists the mutant type and the second row lists the total number of frames in which the worms were moving forward in the 30 videos of that strain. The third row lists the number of detected events declared by the algorithm to be foraging events. The fourth row shows the number of foraging events in 10 s (300 frames). In Table 4, we can see that mutant types *dgk-1* and *goa-1* which are hyperactive for locomotion and foraging have higher foraging rate in 10 s whereas *glr-1* and *trpa-1* forage more slowly than wild type. Furthermore, wild type and *dgk-1* have very close foraging rate in 10 s.

For each strain, we also want to determine whether the foraging behavior is a periodic and continuous oscillation or a process in which foraging movements occur sporadically. Our hypothesis is that the foraging behavior of each strain is an almost periodic process with a certain T between adjacent foraging events. If this is true, we expect all time intervals between adjacent events for each strain to be close to each other and at least locate within a certain range (in this experiment, we use the Interval AVE in Table 3, ± 0.1 s to be our range). We use a Chi-Square test (Glantz, 1996) to compare the expected and observed results from all videos of each strain and the results are listed in Table 4. We can see that all p-values are less than 0.05 (≈ 0) which means the difference between the expected and observed result is significant and the foraging behavior is more or less a sporadic process rather than periodic.

4. Discussion

We have described a new algorithm for the automated detection and quantitative analysis of foraging in *C. elegans*. This algorithm makes it possible to use videos of crawling nematodes collected from an automated tracking system to detect foraging events with a reliability comparable to what is achieved by a human observer. The ability to automatically count the number

Table 5
The results of the significance test (p-value <0.05 is considered to be significant)

	dgk-1(nu62) against wild type	*glr-1(n2361)* against wild type	*goa-1(n1143)* against wild type	*trpa-1(ok999)* against wild type
p-Value (amplitude)	0.0087	0.0187	0.0000	0.0011
p-Value (interval)	0.1129	0.0000	0.0018	0.0234
p-Value (frequency)	0.1556	0.0018	0.0000	0.0003

The second to fourth rows show the p-values for comparisons of amplitude, time interval and frequency, respectively.

of foraging events in a unit time facilitates the rapid quantification of the foraging rate, a key behavioral parameter in a number of previous *C. elegans* studies (Alkema et al., 2005; Kindt et al., 2007; Segalat et al., 1995). In the past, this rate has been calculated by observer analysis of video recordings, a laborious and time-consuming process.

In addition to making it possible to count foraging events, our algorithm also makes it possible to measure parameters of foraging behavior that have not previously been measured quantitatively. For example, we measured foraging amplitude. Previous studies noted anecdotally that abnormalities in specific neurons and genes can affect the depth of foraging bends. For example, it was reported that ablation of two classes of mechanosensory neurons, OLQ and IL1, leads to deeper foraging bends (Hart and Kaplan, 1995), as do mutations in the *trpa-1* gene which encodes a mechanosensory channel that functions in these neurons (Kindt et al., 2007). However, neither of these studies was able to present quantitative data to verify or measure the differences between normal worms and lesioned or mutant animals. In the current study, we quantified the foraging amplitude phenotypes of *trpa-1* mutants as well as several other foraging-abnormal mutants. For example, the average amplitude of *trpa-1* was found to be 15.71 compared to 14.15 for wild type, and this difference was statistically significant at the 5% significance level ($p = 0.0011$). This parameter should prove useful for future analysis of *C. elegans* behavioral mutants affecting the neurons controlling foraging bends.

We also derived two other novel foraging-related parameters in this study. One is foraging frequency. We verified the derived frequencies by using Fourier analysis and the power spectrum of the foraging traces of individual worms. The second parameter is the time interval between adjacent foraging events. Combined with the significance test (t-test) (O'Mahony, 1986), we showed that *dgk*-1 has the closest relationship to wild type among the four mutants. It has two categories (interval and frequency) with p-values greater than 0.05 which is considered to be insignificant while other mutants have none (Table 5). We also used a Chi-Square test to examine whether the observed data are periodic. This result suggests that during periods of active foraging, the foraging behavior is more or less sporadic rather than a process in which foraging movements occur periodically and continuously.

5. Conclusion

The main contributions of this paper can be summarized as follows: (1) we developed and tested a new algorithm for automatic detection of foraging events. (2) We provided quantitative analysis of foraging behavior, which has not previously been achieved, for several mutant types. (3) We verified the existence and quantified the amount of differences in the depth of nose bending between normal worms and lesioned or mutant animals, which was reported only anecdotally in previous studies. In previous studies, foraging events were scored by human observers which is tedious and labor-intensive. The development of automated methods for the study of foraging behaviors makes it possible to reliably detect foraging events and quantitatively parameterize foraging patterns. The algorithms we developed therefore should have significant utility in future studies of foraging behavior.

Acknowledgments

The authors would like to thank the Caenorhabditis Genetics Center for strains, and Kathleen Quast for data collection. This work was supported by a research grants from NIDA (DA18341 and DA12891).

References

Alkema MJ, Hunter-Ensor M, Ringstad N, Horvitz HR. Tyramine functions independently of octopamine in the *Caenorhabditis elegans* nervous system. Neuron 2005;46:247–60.

Avery L, Thomas JH. Feeding and defecation. *C. elegans* II. NY: Cold Spring Harbor; 1997.

Baek J, Cosman P, Feng Z, Silver J, Schafer WR. Using machine vision to analyze and classify *Caenorhabditis elegans* behavioral phenotypes quantitatively. J Neurosci Meth 2002;118:9–21.

Barr MM, Garcia LR. Male mating behavior. WormBook; 2006. http://www.wormbook.org/chapters/www_malematingbehavior/malematingbehavior.html.

Brenner S. The genetics of *Caenorhabditis elegans*. Genetics 1974;77:71–94.

Chen BL, Hall DH, Chklovskii DB. Wiring optimization can relate neuronal structure and function. Proc Natl Acad Sci USA 2006;103:4723–8.

Cronin CJ, Mendel JE, Mukhtar S, Kim YM, Stirbl RC, Bruck J, Sternberg PW. An automated system for measuring parameters of nematode sinusoidal movement. BMC Genet 2005;6:5.

Driscoll M, Kaplan J. Mechanotransduction. *C. elegans* II. NY: Cold Spring Harbor; 1997.

Feng Z, Cronin CJ, Wittig Jr JH, Sternberg PW, Schafer WR. An imaging system for standardized quantitative analysis of *C. elegans* behavior. BMC Bioinformatics 2004;5:115.

Geng W, Cosman P, Berry C, Feng Z, Schafer WR. Automatic tracking, feature extraction and classification of *C. elegans* phenotypes. IEEE Trans Biomed Eng 2004;51:1811–20.

Glantz SA. Primer of biostatistics. 4th ed. McGraw-Hill; 1996.

Gonzalez R, Woods R. Digital image processing. 2nd ed. NJ: Prentice Hall; 2002.

Hart AC, Sims S, Kaplan JM. Synaptic code for sensory modalities revealed by *C. elegans* GLR-1 glutamate receptor. Nature 1995;378:82–5.

Hoy JB, Koehler PG, Patterson RS. A microcomputer-based system for real-time analysis of animal movement. J Neurosci Methods 1996;64:157–61.

Hoy JB, Porter SD, Koehler PG. A microcomputer-based activity meter for multiple animals. J Neurosci Methods 1997;72:183–8.

Huang K, Cosman P, Schafer WR. Machine vision based detection of omega bends and reversals in *C. elegans*. J Neurosci Methods 2006;158:323–36.

Kaplan JM, Horvitz HR. A dual mechanosensory and chemosensory neuron in *Caenorhabditis elegans*. Proc Natl Acad Sci USA 1993;90:2227–31.

Karbowski J, Schindelman G, Cronin CJ, Seah A, Sternberg PW. Systems level circuit model of *C. elegans* undulatory locomotion: mathematical modeling and molecular genetics. J Comput Neurosci 2007;24:253–76.

Kindt KS, Viswanath V, Macpherson L, Quast K, Hu H, Patapoutian A, et al. *Caenorhabditis elegans* TRPA-1 functions in mechanosensation. Nat Neurosci 2007;10:568–77.

Manolakis D, Ingle V, Kogon S. Statistical and adaptive signal processing. McGraw-Hill; 2000.

Metz CE. Basic principles of ROC analysis. Semin Nucl Med 1978;8(4): 283–98.

O'Mahony M. Sensory evaluation of food: statistical methods and procedures. CRC Press; 1986.

Schafer WF. Genetics of egg-laying in worms. Annu Rev Genet 2006;40: 487–509.

Segalat L, Elkes DA, Kaplan JM. Modulation of serotonin-controlled behaviors by G_o in *Caenorhabditis elegans*. Science 1995;267:1648–51.

Welch PW. The use of fast Fourier transform for the estimation of power spectra: a method based on time averaging over short, modified periodograms. IEEE Trans Audio Electroacoust 1967;15(2):70–6.

White J, Southgate E, Thomson J, Brenner S. The structure of the nervous system of the nematode *Caenorhabditis elegans*. Phil Trans R Soc Lond (Biol) 1986;314:1–340.